Position- and Polarization-Specific Waveguiding of Multi-Emissions in Single ZnO Nanorods

Bonghwan Chon[†], *Johnson Truong*[‡], *Matthew Hansen*[‡], *Jong-in Hahm*[‡,*], *Young Jong Lee*[†,*]

[†] Biosystems and Biomaterials Division, National Institute of Standards and Technology, Gaithersburg, MD 20899

[‡] Department of Chemistry, Georgetown University, Washington, DC 20057

ABSTRACT

We examine multiphoton-produced optical signals waveguided through single ZnO nanorods (NRs) using a newly developed, scanning offset-emission hyperspectral microscopy (SOHM) technique. Specifically, we concurrently analyze waveguiding behaviors of sum-frequency generation (SFG), deep-trap emissions (DTE), and coherent anti-Stokes Raman scattering (CARS) occurring in individual ZnO NRs. SOHM acquires spectrally-indexed and spatially-resolved intensity maps/spectra of waveguided light intensity while excitation/emission collection positions and light polarization are scanned. Hence, the powerful measurement capabilities of SOHM enable quantitative analyses of the different ZnO NR waveguiding behaviors specific to the multiphoton-generated emissions as a function of measurement position, light-matter interaction geometry, and the optical origin of the guided signal. We subsequently reveal the distinct waveguiding behaviors of single ZnO NRs pertaining to the SFG-, DTE-, and CARS-originated signals and discuss particularly attractive ZnO NR properties in CARS waveguiding.

KEYWORDS zinc oxide nanorod, waveguiding, deep-trap emission, coherent anti-Stokes Raman scattering, polarization, scanning offset-emission hyperspectral microscopy

Unique optical properties of zinc oxide (ZnO) nanomaterials afford many important optoelectronic and biomedical applications for which nanoscale ZnO materials have been previously constructed into highly miniaturized light-emitting diodes,[1,2,3] lasers,[4,5,6,7] waveguides,[8,9,10,11] and biosensors.[12,13,14] Burgeoning research efforts have made for the discovery and engineering of novel optical properties of ZnO, particularly one-dimensional (1D) ZnO nanomaterials, such as nanorods (NRs) and nanowires (NWs). 1D ZnO nanomaterials have proven attractive as their inherently high shape anisotropy and reduced dimensionality can be exploited to further enhance the materials' unique optical properties, such as extremely directional light propagation/emission and highly localized light delivery/collection.[8,9,10,11,13,14,15,16,17] In this regard, highly efficient excitonic photoluminescence (PL) has been reported for its spontaneous and stimulated emission applications.[4,7,18,19,20] In addition, we have previously identified distinctive Mie and Raman scattering characteristics of intrinsic ZnO NRs[21,22] as well as fluorescence emission properties from fluorophores placed in the vicinity of ZnO NRs.[15,16,17]

Unlike these and many other studies focusing on the linear optical responses of ZnO nanostructures, nonlinear optical properties and waveguiding behaviors of ZnO nanomaterials have not yet been explored as extensively. Yet, previous studies have shown that ZnO NRs exhibit strong second-harmonic generation (SHG) and third-harmonic generation (THG) signals due to NR's large nonlinear susceptibilities in comparison to the bulk and thin film forms of ZnO.[23,24,25,26,27] Compared to the directly observed optical emission behaviors, even fewer studies have been devoted to characterizing light waveguiding through ZnO NRs. Existing works on the waveguiding behaviors of individual ZnO nanostructures mainly examined light propagation of the ZnO excitonic PL and that of the UV/visible light launched from an independent light source.[9,10,24,28] The outcomes from these pioneering works indicate that the waveguiding

characteristics of nanomaterials can be strongly influenced by various factors including the light-matter interaction geometry, the wavelength of light, and the physical dimensions of the materials.[8,15,26,29,30] It can also vary depending on the origins of guided optical signals, as shown in the different guiding behaviors of the band-edge emission versus the defect emission in ZnO.[8,31]

Understanding waveguiding behaviors of multiphoton-generated optical signals through ZnO nanomaterials will be highly beneficial to the development of various integrated nanoscale photonic systems for computing, imaging, and sensing.[8,11] Optical emissions produced via multiphoton excitation, unlike the UV-excited ZnO excitonic emission, can be free from background fluorescence contributions in a biomatrix. Also, higher-order susceptibilities associated with nonlinear mixing processes are typically polarization sensitive, allowing for better-waveguided signal detection via controlling a light-matter interaction geometry. Such knowledge can be particularly useful in biological applications of ZnO, as waveguiding through single ZnO nanomaterials enables high spatial localization for the delivery/collection of light using the nanomaterials. Hence, there is a growing need to fully understand and control the waveguiding behaviors of nonlinear optical signals in ZnO as a function of the various factors mentioned above.

Studying single NR behaviors, instead of those of NR ensembles, is useful for identifying waveguiding behaviors that can be difficult to determine from ensemble-averaged data and important for future miniaturized waveguiding applications using single ZnO NRs. Comprehensive examination of individual NRs requires not only a spatial resolving power for separating waveguided emissions that are offset in position from an excitation location on a single NR but also a spectral resolving power for separately characterizing different emission origins. However, current imaging approaches are not optimized for simultaneously providing multilateral NR waveguiding details in a single measurement. This is mainly because imaging methods

employed to study the nonlinear optical behaviors and waveguiding properties of ZnO NRs so far are more suited for one measurement modality at a time. For example, typical acquisitions of waveguiding images and spectra were carried out for a single emission origin and from a single NR location, often from NR

a NR end position.[8,9,10,24,28] To this end, a multimodal measurement technique is highly warranted which can permit rapid mapping and quantitative analyses of position- and polarization-controlled waveguided signals originating from multiple, nonlinear optical emissions in individual ZnO NRs.

In this paper, we characterize the distinct waveguiding phenomena in single ZnO NRs associated with multiphoton-derived, nonlinear emissions over a large spectral range using a newly developed imaging technique, scanning offset-emission hyperspectral microscopy (SOHM). The multiphoton excitation condition used in this study generates emission bands pertinent to the nonlinear optical processes of sum-frequency generation (SFG), deep-trap emission (DTE), and coherent anti-Stokes Raman scattering (CARS). We demonstrate that the SOHM technique can be successfully used to simultaneously obtain waveguiding maps and spectra for SFG, DTE, and CARS emissions in a spatially and spectrally resolved manner. We ascertain distinct ZnO NR waveguiding behaviors specific to the emission from each nonlinear optical origin and quantitatively determine the effects of excitation/emission collection positions and light-matter interaction geometry on waveguiding of the different nonlinear signals. We subsequently discuss highly intriguing NR waveguiding properties associated with CARS emissions that differ from those of SFG and DTE.

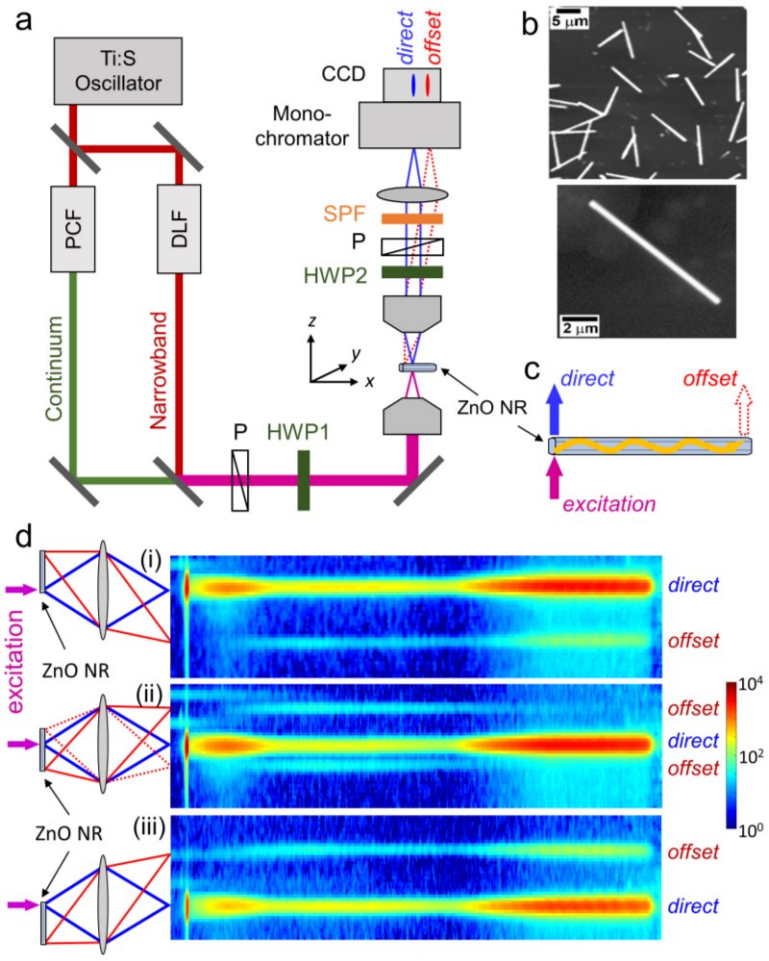

Figure 1. (a) Schematic diagram of the SOHM system: PCF denotes photonic crystal fiber; DLF, dispersionless filter; HWP, half-wave plate; P, polarizer; CCD, charge-coupled device; SPF, short-pass filter. (b) Typical SEM viewgraphs of the as-synthesized ZnO NRs used in our experiments. (c) An illustration displaying the directly emitted signals from the excitation site (denoted as *direct*) and the waveguided emission collected at a shifted position away from the excitation site (denoted as *offset*). (d) CCD images obtained by SOHM showing the *direct* emission and the *offset* emission from a single ZnO NR. The three CCD images were acquired from the same ZnO NR by exciting different positions on the NR as indicated in the diagrams on the left. The vertical axis of the acquired CCD image corresponds to *x*-position along the length of the NR while the horizontal

axis of the CCD image corresponds to the emission wavelength. The excitation polarization was kept perpendicular to the long axis of the ZnO NR for all cases.

RESULTS AND DISCUSSION

Figure 1a displays the overall layout of the key optical components in our home-built SOHM setup to examine different waveguided emissions from individual ZnO NRs with sufficient spatial resolution and spectral range. The overall SOHM setup, inspired by broadband CARS microscopy,[32,33,34] was developed to specifically provide the required measurement capability of simultaneous recording a waveguided emission spectrum from each pixel, i.e. over all offset distances on the NR per each excitation location, using the whole CCD image. ZnO NR samples were prepared by first synthesizing them via a gas-phase approach according to the previously described procedures, which yield highly crystalline, wurtzite ZnO NRs.[14,15,35,36] The scanning electron microscope (SEM) images in Figure 1b display the typical morphology of as-grown ZnO NRs on a Si growth wafer. The ZnO NRs were then dispersed in ethanol via sonication and subsequently transferred onto a glass coverslip before being mounted on a motorized sample stage on the microscope. ZnO NRs are known to exhibit a strong nonlinear susceptibility and great photostability,[23,24,25] making them as ideal nanomaterials for our multiphoton SOHM technique to interrogate their light emission and waveguiding properties.

Figure 1d shows representative emission maps acquired using the SOHM setup described above. The raw CCD images were collected when the excitation beam was focused on three different positions on an identical ZnO NR. The vertical axis of the CCD image corresponds to the *x*-axis in our laboratory coordinate in Figure 1a, i.e., the long axis of the NR, while the horizontal axis

corresponds to the emission wavelength. The *direct* emissions generated at the excitation site appear as the high intensity (yellow-red) horizontal lines. The lower intensity (sky blue-green) lines appearing shifted in the vertical axis of the CCD images correspond to *offset* emissions collected at NR positions away from the excitation site. The SOHM technique can map *offset* emission signals as a function of the offset distance on the NR. The distance-resolved emission lines are marked as *direct* and *offset* next to each SOHM panel belonging to the three different excitation positions of (i), (ii), and (iii).

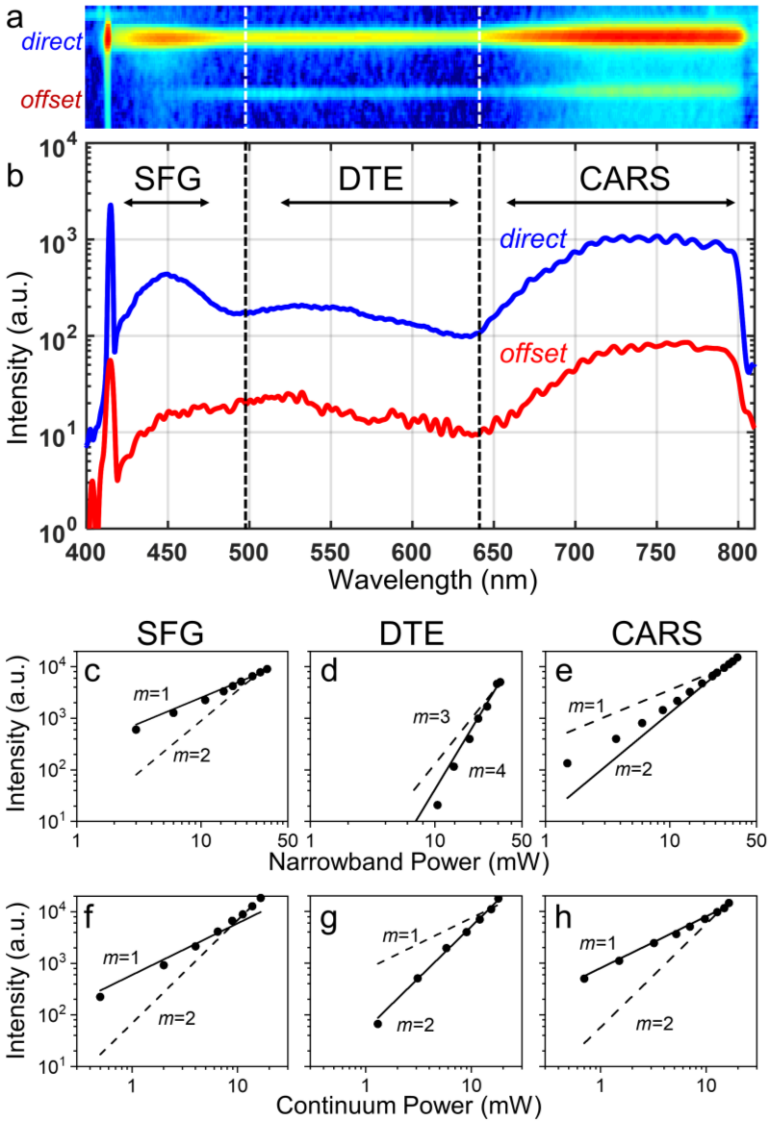

Figure 2. (a,b) Correlated SOHM map and spectra displaying (a) the raw CCD image from the panel (i) in Figure 1d and (b) its *direct* and *offset* emission spectra. (c–h) Log-log plots of the *direct* emission intensity as a function of incident beam powers for the SFG, DTE, and CARS bands. (c–e) *direct* emission intensity as a function of the narrowband power in the presence of the constant continuum power (11 mW). (f–g) *direct* emission intensity as a function of the continuum power in the presence of the constant narrowband power (17 mW). The emission intensities were calculated from averaging the signals in the spectral ranges of 435 nm – 445 nm, 510 nm – 560 nm, and 650 nm – 700 nm for SFG, DTE, and CARS bands, respectively. The power exponent, m, was obtained by power-law fitting, $I_{signal} = c\, I_{laser}^{m}$, where I_{signal} is the observed signal intensity; c, a constant; and I_{laser}, the incident laser power.

Figures 2a and 2b show the CCD image and the corresponding spectra of *direct* and *offset* emissions for the case (i) in Figure 1d, spanning over a broad wavelength range between 400 nm and 800 nm that were simultaneously collected along with the SOHM image. Three distinctive spectral segments can be identified, spanning 400 nm – 500 nm, 500 nm – 640 nm, and 640 nm – 800 nm, as indicated by the vertical dashed lines inserted in the SOHM data in Figures 2a and 2b. We first determine the optical origins of the different emissions observed in the spectral segments. The sharp peak at 415 nm in the first spectral region can be easily identified as the SHG of the 830 nm narrowband beam. This is further confirmed by the second-order power dependence on the intensity of the narrowband light but no response to the continuum light. In the absence of the narrowband light, a weak emission remains at 450 nm – 500 nm, corresponding to the SHG of the 850 nm – 1050 nm continuum light as it showed a second-order power dependence on the continuum. However, these SHG signals lead to frequent CCD saturation for the very strong 415

nm emission and negligible intensities for the weak 450 nm – 500 nm emission. On the other hand, when the two pulses are present together, a relatively strong emission band appears between 420 nm and 470 nm. With its intensity linearly proportional to the power of each pulse as displayed in Figures 2c and 2f, the 420 nm – 470 nm emission can be identified as SFG of the two input pulses. Hence, the first spectral segment in Figure 2b was designated as SFG and this sufficiently strong SFG emission at 420 nm – 470 nm was used as the basis for all quantitative analyses discussed in this paper for the first spectral window.

The second region of 500 nm – 640 nm contains a relatively weak and broad emission band. Its high power dependence on the intensity of the narrowband ($m > 4$) and of the continuum ($m \approx 2$) shown in Figures 2d and 2g, respectively, indicates that high-energy excited states are involved in the emission from this spectral window, similar to the previously reported DTE emission.[8,37] Atomic defects in ZnO such as Zn or O vacancies and interstitial O can result in radiative relaxation from deep levels via DTE.[26,38] The excitation power dependence of the emission signals from the second spectral region of the SOHM data seemed to be consistent with DTE as the wide bandgap of ZnO, 3.37 eV,[4] cannot be reached by a one or two-photon process of the incident beams used in our measurements.

The wavelength range of the last spectral window spanning 640 nm – 800 nm corresponds to that of broadband CARS emission, based on the frequency difference between the narrowband and the continuum beams.[34,39] The measured intensity of the emission band in this spectral region is linearly proportional to the power of the continuum light and squarely proportional to the narrowband power, as shown in Figures 2e and 2h. This further indicates that the two-color CARS generation plays a dominant role in the 640 nm – 800 nm emission.[40] As resonant Raman frequencies of ZnO, lying below 500 cm^{-1}, are outside the detection range of the current SOHM

spectrometer due to the cutoff wavelength of the short-pass filter used to block the incident beams from the detector. Therefore, the featureless 640 nm – 800 nm emission in SOHM is attributed to vibrationally nonresonant CARS emission owing to the nonresonant component of the third-order nonlinear susceptibility of ZnO. Hence, this spectral portion in Figure 2b is denoted as CARS.

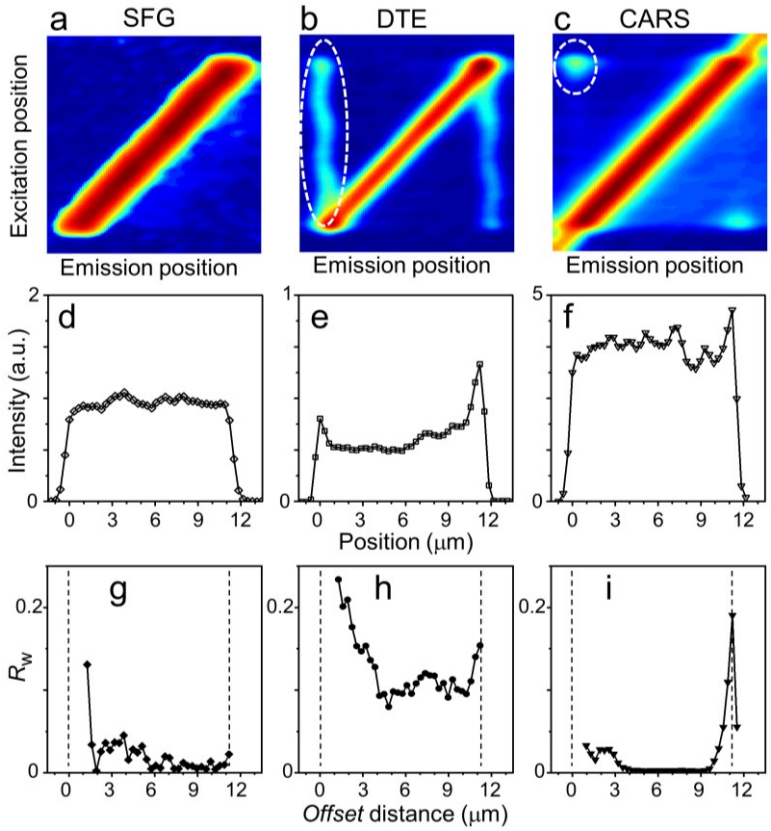

Figure 3. (a–c) 2D intensity maps of the SFG, DTE, and CARS emissions reconstructed from the SOHM data taken on a ZnO NR as a function of excitation position as well as waveguided emission collection position on the NR. The image size is 15 μm x 15 μm. The diagonal line in the 2D map indicates the *direct* emission intensity, whereas the off-diagonal regions represent the waveguided signals emitted at an offset position away from the excitation site. All measurements were performed while keeping the excitation polarization perpendicular to the long axis of the ZnO NR.

(d–f) The intensity of the *direct* emission was profiled as a function of the excitation position. This corresponds to the intensity measured along the diagonal line shown in the 2D maps. (g–i) The waveguiding ratios, R_w, determined from the *direct* and *offset* intensities of the SFG, DTE, and CARS signals are plotted as a function of *offset* distance, separation between excitation and emission collection positions on the NR. The emission intensity data shown correspond to the average intensity values in the spectral regions of 420 nm – 445 nm, 522 nm – 620 nm, and 750 nm – 775 nm for SFG, DTE, and CARS bands, respectively.

Next, we examined the *direct* and *offset* emission profiles of the SFG, DTE, and CARS signals spatially resolved along a single ZnO NR. We observed waveguided *offset* emission signals only from certain positions, rather than all positions on the NR. This phenomenon can be clearly seen in Figure 1c as distinct *offset* emission lines vertically shifted from the *direct* emission line. This, in turn, indicated that *offset* emission signals can be detected only from particular points away from the site of excitation on the NR. Also, based on SOHM maps in Figure 1d, waveguiding of the emitted signals through the ZnO NR seems to proceed efficiently to the NR end(s) with negligible leaking through the NR main body.

For quantitative analyses of such waveguiding behaviors associated with SFG, DTE, and CARS emissions, we collected SOHM intensity maps while controlling the excitation position on a single ZnO NR. The relative intensities between *direct* and *offset* signals corresponding to the SFG, DTE, and CARS emissions in SOHM were subsequently quantified. Figure 3 displays a representative set of the excitation/emission position-resolved, NR-waveguiding results for SFG, DTE, and CARS emission bands obtained from a ZnO NR. The vertical and horizontal axes of the 2D maps represent the excitation and collection positions, respectively. Thus, the diagonal points in the 2D

maps correspond to the emission intensities collected straight from the excitation locations and are the *direct* emission intensities from each scanned position on the NR. These *direct* emission intensity profiles in the 2D maps were plotted as a function of the excitation position on the NR in Figures 3d, 3e, and 3f whose overall magnitudes were found to be the highest to lowest for the CARS, SFG, and DTE signals.

All other off-diagonal points in the 2D intensity maps in Figure 3a correspond to *offset* emissions. The position-dependent waveguiding behaviors of the ZnO NR pertaining to the three emission origins can be qualitatively discerned by examining their *offset* emission behaviors in the 2D maps. The SFG 2D map yielded no detectable off-diagonal signals regardless of the excitation position scanned on the NR, indicating that waveguiding of SFG signals did not effectively take place along the ZnO NR. The DTE *offset* emission can be characterized by the two vertical lines as denoted with a white dashed ellipse in the 2D map. This suggests that DTE signals are waveguided to the distal NR end(s) irrespective of the excitation position on the NR. The *offset* emission of CARS is localized only at the two off-diagonal corners corresponding to the two ends of the NR. The highly localized *offset* emissions, marked with a white circle in the 2D map, indicate that waveguiding of the CARS signals occurs exclusively from one end to the other end and that the CARS signals generated at a non-terminal excitation position are not waveguided effectively. These distinctive waveguiding behaviors of each optical origin are schematically depicted under each position-resolved SOHM map in Figure 3a.

For more quantitative investigations of the distinct waveguiding characteristics associated with the three nonlinear optical emissions from individual ZnO NRs, the waveguided intensities measured at one terminal position of the NR are compared to the intensity measured directly at the excitation point by defining a waveguiding ratio, $R_w = I_{offset}/I_{direct}$, where I_{offset} and I_{direct} are the

offset and *direct* emission intensities, respectively. The R_w values for the three different types of emissions guided by the NR are displayed in Figures 3g–3i as a function of the separation distance between the excitation and emission collection positions on the NR. The different, optical process-specific waveguiding properties of the ZnO NR are clearly seen in the plots. R_w values remained consistently low for SFG over all separation distances of excitation and emission collection on the NR. On the contrary, DTE and CARS emissions exhibit measurable R_w values through the NR. However, the waveguided DTE is nearly constant over the separation distance whereas CARS signals are observed only at the distance equivalent to the full NR length. The non-zero R_w value independent of the separation distance for DTE in Figure 3h indicates that the entrance coupling, i.e., a coupling of emission signals generated at the excitation point into the NR cavity for subsequent waveguiding, is position-insensitive for DTE. Regardless of the excitation position on the NR, a constant amount of DTE photons seem to couple into the NR and subsequently waveguided through the NR towards the NR ends without noticeable attenuation in waveguided emission intensity. In contrast, waveguiding of CARS signals are highly sensitive to the entrance coupling position on the NR, leading to a highly intriguing NR waveguiding property of the peaked R_w at the maximum separation distance with near zero at all other separation distances. This is a clear indication that, only when the excitation and the subsequent entrance coupling into the NR are originated from one of the two end positions of the NR, the CARS signals can be effectively waveguided by the NR with their exit coupling allowed only at the distal end of the NR.

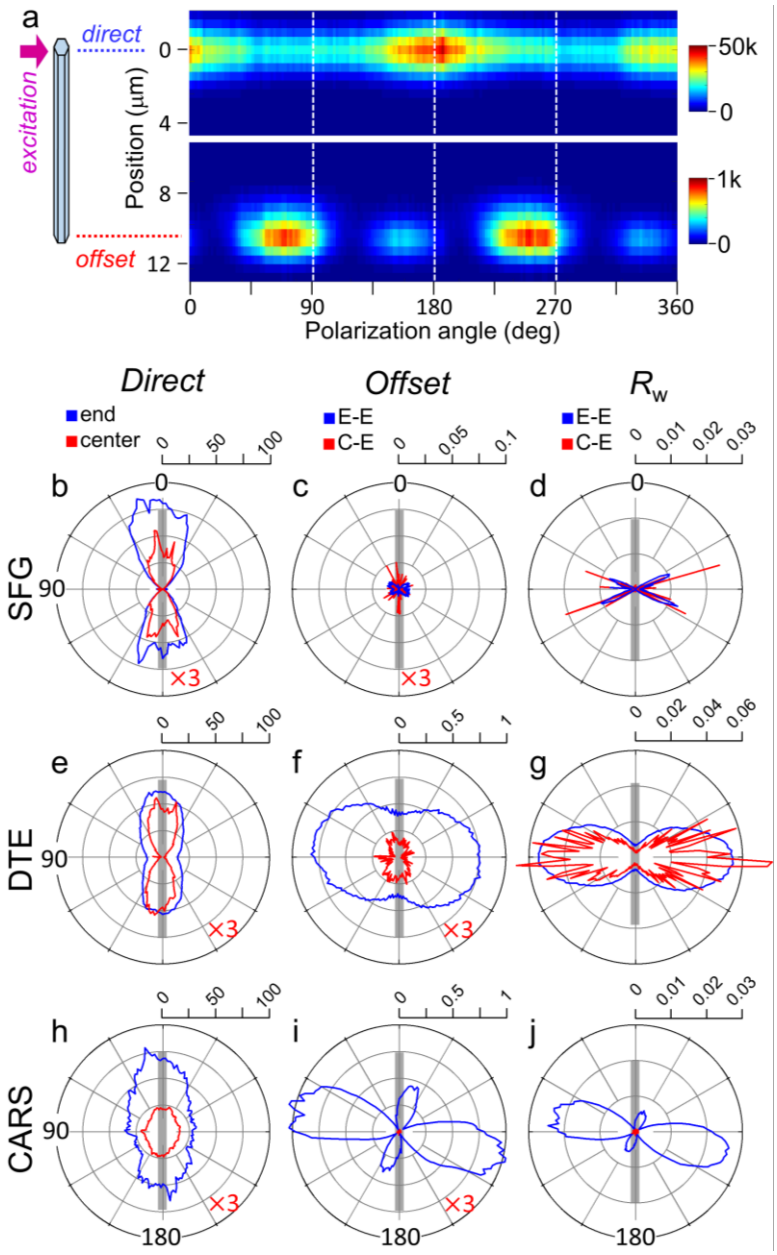

Figure 4. (a) A 2D map of *direct* (the upper panel) and *offset* (the lower panel) waveguided signal intensity of CARS as a function of light polarization angle and emission collection position on a single ZnO NR. Polar plots of the *direct* emission (b, e, h), the *offset* emission (c, f, i), and the waveguiding ratio of R_w (d, g, j) were recorded as a function of angle between light polarization and the ZnO NR long axis for the NR-waveguided emission signals of SFG, DTE, and CARS. Light polarization parallel to the ZnO NR long axis was set to zero. The blue and red data in the

polar plots of *direct* emission display the intensities collected when the excitation position was either the end or center of the NR, respectively. The blue and red lines in polar plots of *offset* emission and R_w display data collected from the waveguiding cases of end-to-end (E-E) and center-to-end (C-E), respectively.

Next, we investigate the effect of light polarization on the NR waveguiding properties for emissions belonging to the three optical origins. SOHM measurements were carried out on single NRs under varying incident polarization angles relative to the NR long axis. The two half-wave plates, one at the excitation and the other at the collection sides, were rotated synchronously, allowing for the detection of only the emitted signals parallel to the incident polarization. For each optical origin, the polarization-controlled and offset distance-resolved waveguiding characteristics of single ZnO NRs are subsequently discerned by simultaneously observing the *direct* and *offset* emissions from the NRs. Results from an exemplary, CARS waveguiding measurement case of E-E which involved excitation at one NR end and emission collection on the other NR are presented as 2D maps in Figure 4a. The mapped data of CARS waveguiding in Figure 4a demonstrates another useful capability of SOHM which can be employed to simultaneously map *direct* and *offset* emission intensities along individual ZnO NRs as a function of light polarization and offset distance.

We then scrutinize the effect of light polarization on *direct* versus *offset* emissions measured from individual ZnO NRs. The results are displayed in Figure 4 for the two cases of end-to-end (E-E) and center-to-end (C-E) waveguiding. The polar plots in Figures 4b, 4e, and 4h show the *direct* emission intensities of SFG, DTE, and CARS signals, respectively, as a function of polarization angle. The vertical axis in all polar plots displayed in Figures 4 corresponds to the

incident light polarized parallel to the NR long axis. Although the polarization aspect (PA) ratio, the maximum-to-minimum intensity ratio obtained when changing polarization angles, varies depending on the optical origin and the excitation position on the NR, the observed intensities for all *direct* emissions are generally stronger for light polarization parallel than perpendicular to the NR long axis. This overall trend is seen from the dipole-shaped polar plots in Figures 4b, 4e, and 4h. The very high PA for SFG *direct* emission and the relatively lower PA for CARS *direct* emission in Figures 4b and 4h, respectively, are consistent with the previous reports on the second- and third-order nonlinear susceptibilities of ZnO.[24,26,41] Among the second-order susceptibilities for wurtzite ZnO, $\chi_{xxx}^{(2)}$ and $\chi_{xyy}^{(2)}$ are allowed as non-zero components from which only the $\chi_{xxx}^{(2)}$ component can further contribute to the *direct* emission signal observed at parallel polarization in our measurement configuration. This can lead to the observed dipolar plots for SFG *direct* emission strongly polarized along the *x*-axis, i.e., the NR long axis, with a very narrow waist. Comparatively, the CARS *direct* emission profile exhibiting a much wider waist reflects that the parallel $\chi_{xxxx}^{(3)}$ component of the third-order susceptibility tensor is only slightly larger than the perpendicular components of $\chi_{yyyy}^{(3)}$ and $\chi_{zzzz}^{(3)}$. A similar result was previously reported which showed that the parallel and perpendicular components of the effective third-order susceptibility in ZnO micro/nanowires are comparable to each other.[26] Hence, the polarization dependences for the *direct* SFG and CARS emissions are strongly dominated by the symmetry of their nonlinear susceptibilities. Unlike these, the polarization profile of DTE *direct* emission can be explained by linear polarization effects such as anisotropic attenuation of the electric field by the high dielectric contrast of NRs similar to what was observed in PL from other NWs.[33]

We subsequently examine the effect of light polarization on the *offset* signals pertaining to the SFG, DTE, and CARS emissions waveguided by the ZnO NR. The polarization-dependent *offset*

emissions are strongly affected by the optical origin and the excitation location, as evidenced in the polar plots in Figures 4c, 4f, and 4i. The *offset* emission polar profiles are rotated perpendicular to those of the corresponding *direct* emissions. This is because, upon coupling of the *xy*-plane-lying emitted signals into the NR at the excitation site, the *xy*-polarization plane needs to be rotated to be in the *yz*-plane for further propagation of the waveguided signals along the NR long axis (*x*-axis). The SFG *offset* emissions for both the C-E and E-E waveguiding cases are very weak, as shown in Figure 4c. The highly *x*-polarized, *direct* emission of SFG at the excitation site might result in very weak entrance coupling into the NR due to a mismatch between the polarization direction of the generated light (the *x*-axis) and the allowed polarization direction (the *y*- and *z*-axes) for propagation along the NR. In comparison, considerable polarization dependences are observed from the *offset* emissions of DTE (Figure 4f) and CARS (Figure 4i), respectively.

In particular, the CARS *offset* emission is found to be highly position- and polarization-dependent. The *direct* emission of CARS shows the most *y*-polarized components out of the three optical origin cases. The non-negligible, *y*-polarized fraction of the generated signal might enable better entrance coupling into the NR, yielding the substantial *offset* emission intensities. The polar plot for the E-E CARS *offset* emission exhibits two dipoles with narrow waists, whereas the C-E CARS *offset* emission is extremely weak. The outcomes indicated that CARS waveguiding through the ZnO NR is highly spatially controlled with its waveguiding allowed for only E-E. In addition, the polar profile of the CARS *offset* emission also reveals a distinct CARS waveguiding nature of the ZnO NR where light-matter interaction becomes particularly important. Displaying the least polarization-dependence of *direct* emission among the three optical origins, CARS emission shows high polarization dependence for its *offset* emission of the waveguided signals through the ZnO NR. Along with the highly spatially-controlled and position-dependent CARS

waveguiding, the waveguiding characteristics of strongly polarization-dependent CARS are newly identified from the ZnO NR. This level of polarization and position dependence is not observed from waveguiding of the DTE- or SFG-derived emissions even though their polar profiles of *direct* emissions display higher polarization dependence relative to CARS.

The polar plots in Figures 4d, 4g, and 4j present polarization-dependent R_w values calculated using the *direct* and *offset* emission intensities measured at each polarization angle. The R_w polar plots of in Figure 4d show interesting shapes but are not discussed because the SFG R_w values are not quantitatively analyzable due to the very low *offset* emission intensities for both C-E and E-E. For DTE, the R_w profiles for E-E and C-E waveguiding in Figure 4g are similar in shape and magnitude with their orientations perpendicular to the NR long axis. The similarity indicates that the different polarization states in waveguided DTE signals are similarly affected by the processes of entrance coupling, transport, and exit coupling for the end versus center excitation cases of E-E and C-E. Unlike those of SFG and DTE, the R_w profile of CARS reveals a distinct polarization-dependent property of the NR in CARS waveguiding. Overall, the R_w values of C-E CARS waveguiding are negligible, but those of E-E CARS waveguiding are substantial, displaying strong polarization dependence in Figure 4j. The clear difference between the C-E and E-E CARS waveguiding profiles suggests that the entrance coupling of CARS emission into a NR is selective to specific polarization states, as confirmed by the high PA of the CARS polarization profile. Although, so far, our discussion has been focused on the specific polarization direction of each emission, it must be noted that the wavelength difference from 400 nm to 800 nm can affect overall waveguiding efficiency. However, the non-monotonic behavior in the polarization dependence and the R_w values shown in Figures 4 and 5, respectively, indicate that the wavelength effect cannot solely explain the observed waveguiding features of broad emission from different origins.

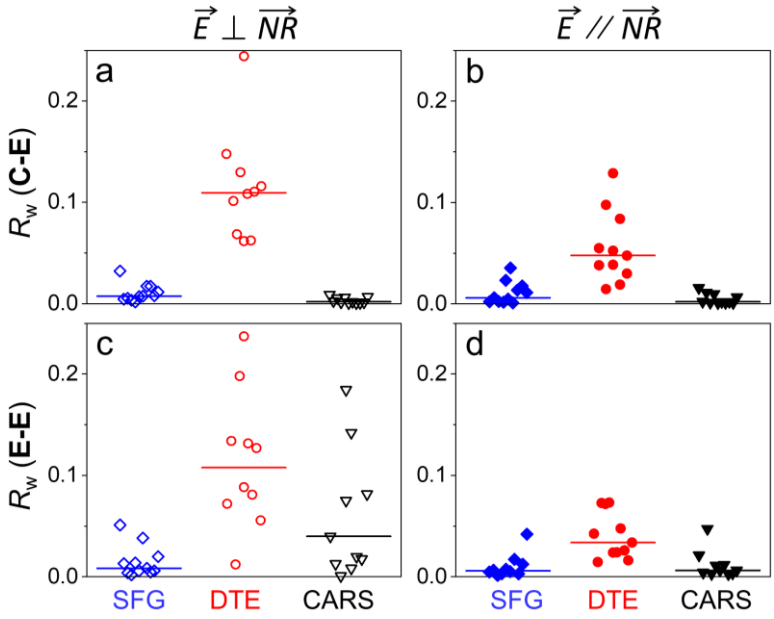

Figure 5. Distributions of waveguiding ratio, R_w, of the eleven isolated NRs measured for three different emission origins. A set of R_w from each NR was determined for the parallel and perpendicular light polarization as well as for C-E and E-E waveguiding cases. The horizontal lines inserted among each data set represent the median of R_w values of the data set.

The distinct emission waveguiding nature of individual ZnO NRs in response to the different optical origins was further confirmed by examining ten more isolated ZnO NRs via SOHM. R_w values for the three different emission bands are determined from the additional NRs using their respective *direct* and *offset* emission intensities measured for the parallel and perpendicular polarization cases under the C-E and E-E waveguiding settings. The results are summarized in Figure 5 for the different measurement situations. As seen from the additional NR data, the general trend in their waveguiding characteristics further substantiates the SOHM results discussed earlier for the SFG, DTE, and CARS emissions. Substantial DTE and CARS signals are effectively guided

through single ZnO NRs whereas SFG emissions are only weakly guided. The waveguided emission intensities are typically below 20 % of the directly emitted signals measured right at the excitation point for DTE and CARS, while less than 2 % guiding occurs for SFG. Overall, emission waveguiding through individual ZnO NRs is more effective under perpendicular than parallel polarization, especially for the CARS-originated emissions. The interesting nature of CARS waveguiding in ZnO NRs further suggests that the measured CARS emissions from ZnO NRs can be attributed to signals derived exclusively from emission sources at the NR ends with negligible contributions from other potential sources on other NR parts or in the NR surrounding, even under a far-field excitation situation. If employed as a highly spatially localized bioprobe, this unique NR waveguiding property, in turn, can be exploited to collect only the CARS signals generated from an analyte at the NR termini with minimal background contributions. Hence, the distinct CARS waveguiding property of ZnO NRs newly identified in this study may be particularly beneficial to Raman-based, biomedical detection, and sensing applications. In addition, the SOHM technique can be broadly useful in the optimization of nanomaterials for efficient nanophotonics and optical communication. If systematically extended to a study of CARS resonant and nonresonant signals in other well-defined nanomaterials, such as carbon nanotubes,[42] graphenes,[43] and monolayer molybdenum disulfide,[44] SOHM may provide insight into the detailed waveguiding mechanism of those nanomaterials whose processes are highly sensitive to a given geometry of light-matter interaction.

CONCLUSION

We have demonstrated that SOHM can be effectively used to reveal the distinctive ZnO NR waveguiding properties for the SFG, DTE, and CARS emissions. The newly developed technique

enables simultaneous detection and quantification of *direct* and *offset* emissions from individual ZnO NRs while systematically scanning the excitation/emission collection positions on the NR and controlling light polarization directions. Owing to these capabilities, we have ascertained the polarization- and position-dependent, ZnO NR waveguiding properties unique to each nonlinearly generated, optical emission. We observe substantial waveguiding of DTE and CARS signals and very weak SFG guiding through ZnO NRs. DTE shows waveguided emissions at the NR ends regardless of the excitation position on the NR. However, waveguiding of CARS only occurs for E-E, i.e. exclusively for the case of excitation at one NR end and collection at the distal end. Waveguided CARS intensities are negligible when all other NR positions are used for excitation/emission collection. Overall, *direct* emission profiles show polarization dependence in the descending order of SFG, DTE, and CARS. For the waveguided *offset* emissions, CARS exhibited very strong polarization dependence followed by DTE. With SOHM, we have revealed the fact that ZnO NRs are capable of waveguiding CARS emissions, which has never been reported before. We also have identified the distinctive CARS waveguiding nature through single ZnO NRs, exhibiting high position- and polarization-dependence. Beyond ZnO NRs demonstrated here, SOHM may have a broader utility in similarly quantifying position- and polarization-resolved waveguiding characteristics of broadband emissions from other technologically important nanomaterials in a rapid and parallel fashion. Also, this unique imaging method can be used to investigate not only the overall waveguiding efficiency but also the underlying waveguiding mechanisms that are closely related to the intrinsic optical properties of the sample material, such as nonlinear susceptibilities and optical anisotropy.

METHODS

Sample preparation

In brief, NR growths were carried out on a Si wafer substrate (Silicon Quest International Inc., San Jose, CA) containing pre-deposited 20 nm Au colloids (Ted Pella, Inc., Redding, CA.) as catalysts. The source materials of a 2:1 mixture of graphite (99%, VWR International, LLC) to ZnO powders (99.999%, Alfa Aesar, Inc.) were placed in a quartz boat at the center of a horizontal tube furnace. A target boat containing the catalyst-deposited Si growth wafer was placed at approximately 15 cm downstream. The furnace was then heated to 850-950 °C for 15-35 min at a ramp up/ramp down rate of 15°C/min under a constant Ar flow of 100 standard cubic centimeters per minute. As-synthesized ZnO NRs were sonicated off from the growth substrate and dispersed in ethanol. A drop-wise deposition of the ZnO NRs in ethanol onto a clean coverslip led to NRs lying flat on the coverslip surface. The SEM images were obtained on an FEI/Philips XL 20 SEM on a Si growth wafer.

Scanning offset-emission hyperspectral microscopy (SOHM)

A fundamental laser beam from a Ti:Sapphire femtosecond oscillator (MaiTai, Spectra-Physics), centered at 830 nm with the bandwidth of 14 nm, was split into two beams. One beam was spectrally narrowed to 1 nm by a 4-*f* dispersionless filter. The other beam was introduced into a photonic crystal fiber (Femtowhite, NKT Photonics) to produce a continuum light ranging from 850 nm to 1150 nm after a long-pass filter. The two beams were combined and directed collinearly toward the sample. The polarizations of the two beams were linear and parallel to each other, and their polarization was controlled by an achromatic half-wave plate (AHWP05M-980, Thorlabs). The excitation beams were subsequently focused onto a ZnO NR of interest through an objective lens (40X, numerical aperture (NA) 0.95, Olympus). The laser powers measured at the sample

location were approximately 17 mW and 11 mW for the narrowband and the continuum, respectively. The emission signals generated from the NR were then collimated by a collecting objective lens (60x, NA 0.7, Olympus) in the forward direction. The signals were directed to another achromatic half-wave plate (AHWP05M-600, Thorlabs), then to an 810 nm short-pass filter, and finally analyzed by an astigmatism-corrected monochromator (IsoPlane SCT-320, Princeton Instruments) equipped with a charge-coupled device (CCD) camera (1024 x 256 pixels, DU920-BRDD, Andor). For the SOHM measurement, the excitation beams were scanned along the length of the NR using the motorized sample stage while direct and waveguided emission signals were monitored over the entire NR. SOHM data were acquired and analyzed using an in-house developed LabView program and MATLAB codes

Corresponding Authors

*YJL: youngjong.lee@nist.gov; JIH: jongin.hahm@georgetown.edu.

Notes

The authors declare no competing financial interest.

Certain commercial equipment, instruments, or materials are identified in this paper to foster understanding. Such identification does not imply endorsement by NIST, nor does it imply that the materials or equipment identified are necessarily the best available for the purpose.

ACKNOWLEDGMENT

The authors acknowledge the financial support of this work by the National Science Foundation (Award No CBET1841373) from the Chemical, Bioengineering, Environmental and Transport Systems Division under the Directorate for Engineering.

REFERENCES

1. Bao, J.; Zimmler, M. A.; Capasso, F.; Wang, X.; Ren, Z. F., Broadband ZnO Single-Nanowire Light-Emitting Diode. *Nano Lett.* **2006,** *6*, 1719-1722.
2. Manekkathodi, A.; Lu, M. Y.; Wang, C. W.; Chen, L. J., Direct Growth of Aligned Zinc Oxide Nanorods on Paper Substrates for Low-Cost Flexible Electronics. *Adv. Mater.* **2010,** *22*, 4059-4063.
3. Zimmler, M. A.; Stichtenoth, D.; Ronning, C.; Yi, W.; Narayanamurti, V.; Voss, T.; Capasso, F., Scalable Fabrication of Nanowire Photonic and Electronic Circuits Using Spin-on Glass. *Nano Lett.* **2008,** *8*, 1695-1699.
4. Gargas, D. J.; Gao, H.; Wang, H.; Yang, P., High Quantum Efficiency of Band-Edge Emission from ZnO Nanowires. *Nano Lett.* **2011,** *11* (9), 3792-3796.
5. Huang, M. H.; Mao, S.; Feick, H.; Yan, H.; Wu, Y.; Kind, H.; Weber, E.; Russo, R., Room-Temperature Ultraviolet Nanowire Nanolasers. *Science* **2001,** *292*, 1897-1899.
6. van Vugt, L. K.; Rühle, S.; Vanmaekelbergh, D., Phase-Correlated Nondirectional Laser Emission from the End Facets of a ZnO Nanowire. *Nano Lett.* **2006,** *6* (12), 2707-2711.
7. Zhang, C.; Zhang, F.; Xia, T.; Kumar, N.; Hahm, J.; Liu, J.; Wang, Z. L.; Xu, J., Low-threshold Two-photon Pumped ZnO Nanowire Lasers. *Opt. Express* **2009,** *17* (10), 7893-7900.
8. Johnson, J. C.; Yan, H.; Yang, P.; Saykally, R. J., Optical Cavity Effects in ZnO Nanowire Lasers and Waveguides. *J. Phys. Chem. B* **2003,** *107*, 8816-8828.
9. Law, M.; Sirbuly, D. J.; Johnson, J. C.; Goldberger, J.; Saykally, R. J.; Yang, P., Nanoribbon Waveguides for Subwavelength Photonics Integration. *Science* **2004,** *305*, 1269-1273.
10. Voss, T.; Svacha, G. T.; Mazur, E.; Müller, S.; Ronning, C.; Konjhodzic, D.; Marlow, F., High-Order Waveguide Modes in ZnO Nanowires. *Nano Lett.* **2007,** *7*, 3675-3680.
11. Michalsky, T.; Wille, M.; Grundmann, M.; Schmidt-Grund, R., Spatiotemporal Evolution of Coherent Polariton Modes in ZnO Microwire Cavities at Room Temperature. *Nano Lett.* **2018**.
12. Hahm, J., Fundamental Properties of One-Dimensional Zinc Oxide Nanomaterials and Implementations in Various Detection Modes of Enhanced Biosensing. *Ann. Rev. Phys. Chem.* **2016,** *67*, 691-717.
13. Singh, M.; Alabanza, A.; Gonzalez, L. E.; Wang, W.; Reeves, W. B.; Hahm, J., Ultratrace Level Determination and Quantitative Analysis of Kidney Injury Biomarkers in Patient Samples Attained by Zinc Oxide Nanorods. *Nanoscale* **2016,** *8*, 4613-4622.
14. Yan, R.; Park, J.-H.; Choi, Y.; Heo, C.-J.; Yang, S.-M.; Lee, L. P.; Yang, P., Nanowire-Based Single-Cell Endoscopy. *Nat. Nanotechnol.* **2012,** *7* (3), 191-196.
15. Singh, M.; Jiang, R.; Coia, H.; Choi, D. S.; Alabanza, A.; Chang, J. Y.; Wang, J.; Hahm, J., Insight into Factors Affecting the Presence, Degree, and Temporal Stability of Fluorescence Intensification on ZnO Nanorod Ends. *Nanoscale* **2015,** *7*, 1424-1436.
16. Singh, M.; Song, S.; Hahm, J., Unique Temporal and Spatial Biomolecular Emission Profile on Individual Zinc Oxide Nanorods. *Nanoscale* **2014,** *6*, 308-315.
17. Truong, J.; Singh, M.; Hansen, M.; Hahm, J., Polarization-Resolved Mechanistic Investigation of Fluorescence Signal Intensification on Zinc Oxide Nanorod Ends. *Nanoscale* **2017,** *9* (24), 8164-8175.
18. Wang, X.; Summers, C. J.; Wang, Z. L., Large-Scale Hexagonal-Patterned Growth of Aligned ZnO Nanorods for Nano-optoelectronics and Nanosensor Arrays. *Nano Lett.* **2004,** *4* (3), 423-426.

19. Rühle, S.; van Vugt, L. K.; Li, H. Y.; Keizer, N. A.; Kuipers, L.; Vanmaekelbergh, D., Nature of Sub-Band Gap Luminescent Eigenmodes in a ZnO Nanowire. *Nano Lett.* **2008,** *8* (1), 119-123.
20. Schirra, M.; Feneberg, M.; Prinz, G. M.; Reiser, A.; Röder, T.; Thonke, K.; Sauer, R., Beating of Coupled Ultraviolet Light Modes in Zinc Oxide Nanoresonators. *Phys. Rev. Lett.* **2009,** *102* (7), 073903.
21. Choi, D. S.; Singh, M.; Zhou, H.; Milchak, M.; Hahm, J., Scattering Attributes of One-dimensional Semiconducting Oxide Nanomaterials Individually Probed for Varying Light-matter Interaction Angles. *Appl. Phys. Lett.* **2015,** *107* (15), 151110.
22. Hansen, M.; Truong, J.; Xie, T.; Hahm, J., Spatially Distinct Raman Scattering Characteristics of Individual ZnO Nanorods under Controlled Polarization: Intense End Scattering from Forbidden Modes. *Nanoscale* **2017,** *9* (24), 8470-8480.
23. Das, S. K.; Bock, M.; O'Neill, C.; Grunwald, R.; Lee, K. M.; Lee, H. W.; Lee, S.; Rotermund, F., Efficient Second Harmonic Generation in ZnO Nanorod Arrays with Broadband Ultrashort Pulses. *Appl. Phys. Lett.* **2008,** *93*, 3-5.
24. Johnson, J. C.; Yan, H.; Schaller, R. D.; Petersen, P. B.; Yang, P.; Saykally, R. J., Near-Field Imaging of Nonlinear Optical Mixing in Single Zinc Oxide Nanowires. *Nano Lett.* **2002,** *2*, 279-283.
25. Neeman, L.; Ben-Zvi, R.; Rechav, K.; Popovitz-Biro, R.; Oron, D.; Joselevich, E., Crystallographic Mapping of Guided Nanowires by Second Harmonic Generation Polarimetry. *Nano Lett.* **2017,** *17* (2), 842-850.
26. Wang, K.; Zhou, J.; Yuan, L.; Tao, Y.; Chen, J.; Lu, P.; Wang, Z. L., Anisotropic Third-Order Optical Nonlinearity of a Single ZnO Micro/Nanowire. *Nano Lett.* **2012,** *12*, 833-838.
27. Mehl, B. P.; House, R. L.; Uppal, A.; Reams, A. J.; Zhang, C.; Kirschbrown, J. R.; Papanikolas, J. M., Direct Imaging of Optical Cavity Modes in ZnO Rods Using Second Harmonic Generation Microscopy. *J. Phys. Chem. A* **2010,** *114* (3), 1241-1246.
28. Sirbuly, D. J.; Law, M.; Pauzauskie, P.; Yan, H.; Maslov, A. V.; Knutsen, K.; Ning, C.-Z.; Saykally, R. J.; Yang, P., Optical Routing and Sensing with Nanowire Assemblies. *Proc. Nat. Acad. Sci. USA* **2005,** *102* (22), 7800-7805.
29. Wang, J.; Gudiksen, M. S.; Duan, X.; Cui, Y.; Lieber, C. M., Highly Polarized Photoluminescence and Photodetection from Single Indium Phosphide Nanowires. *Science* **2001,** *293*, 1455-1457.
30. Börner, S.; Rüter, C. E.; Voss, T.; Kip, D.; Schade, W., Modeling of ZnO Nanorods for Evanescent Field Optical Sensors. *Phys. Stat. Sol. (a)* **2007,** *204* (10), 3487-3495.
31. House, R. L.; Kirschbrown, J. R.; Mehl, B. P.; Gabriel, M. M.; Puccio, J. A.; Parker, J. K.; Papanikolas, J. M., Characterizing Electron–Hole Plasma Dynamics at Different Points in Individual ZnO Rods. *J. Phys. Chem. C* **2011,** *115* (43), 21436-21442.
32. Camp, C. H.; Lee, Y. J.; Cicerone, M. T., Quantitative, Comparable Coherent anti-Stokes Raman Scattering (CARS) Spectroscopy: Correcting Errors in Phase Retrieval. *J. Raman Spectrosc.* **2016,** *47* (4), 408-415.
33. Gohad, N. V.; Aldred, N.; Hartshorn, C. M.; Lee, Y. J.; Cicerone, M. T.; Orihuela, B.; Clare, A. S.; Rittschof, D.; Mount, A. S., Synergistic Roles for Lipids and Proteins in the Permanent Adhesive of Barnacle Larvae. *Nat. Commun.* **2014,** *5*, 4414.
34. Lee, Y. J.; Parekh, S. H.; Kim, Y. H.; Cicerone, M. T., Optimized Continuum from a Photonic Crystal Fiber for Broadband Time-Resolved Coherent Anti-Stokes Raman Scattering. *Opt. Express* **2010,** *18*, 4371-4379.

35. Singh, M.; Zhuo, X.; Choi, D. S.; Gonzalez, L. E.; Wang, J.; Hahm, J., Effects of Crystallographic Facet-Specific Peptide Adsorption along Single ZnO Nanorods on the Characteristic Fluorescence Intensification on Nanorod Ends (FINE) Phenomenon. *Nanoscale* **2015,** *7* (44), 18813-18826.
36. Gargas, D. J.; Moore, M. C.; Ni, A.; Chang, S. W.; Zhang, Z.; Chuang, S. L.; Yang, P., Whispering Gallery Mode Lasing from Zinc Oxide Hexagonal Nanodisks. *ACS Nano* **2010,** *4*, 3270-3276.
37. Vanheusden, K.; Warren, W. L.; Seager, C. H.; Tallant, D. R.; Voigt, J. A.; Gnade, B. E., Mechanisms Behind Green Photoluminescence in ZnO Phosphor Powders. *J. Appl. Phys.* **1996,** *79*, 7983-7990.
38. Djurišić, A. B.; Leung, Y. H.; Tam, K. H.; Hsu, Y. F.; Ding, L.; Ge, W. K.; Zhong, Y. C.; Wong, K. S.; Chan, W. K.; Tam, H. L.; Cheah, K. W.; Kwok, W. M.; Phillips, D. L., Defect Emissions in ZnO Nanostructures. *Nanotechnol.* **2007,** *18* (9), 095702.
39. Ryu, I. S.; Camp, C. H.; Jin, Y.; Cicerone, M. T.; Lee, Y. J., Beam scanning for Rapid Coherent Raman Hyperspectral Imaging. *Opt. Lett.* **2015,** *40*, 5826.
40. Lee, Y. J.; Liu, Y.; Cicerone, M. T., Characterization of Three-Color CARS in a Two-Pulse Broadband CARS Spectrum. *Opt. Lett.* **2007,** *32*, 3370.
41. Chan, S. W.; Barille, R.; Nunzi, J. M.; Tam, K. H.; Leung, Y. H.; Chan, W. K.; Djurišić, A. B., Second Harmonic Generation in Zinc Oxide Nanorods. *Appl. Phys. B: Lasers Opt.* **2006,** *84*, 351-355.
42. Tomita, K.; Kojima, Y.; Kannari, F., Selective Coherent Anti-Stokes Raman Scattering Microscopy Employing Dual-Wavelength Nanofocused Ultrafast Plasmon Pulses. *Nano letters* **2018,** *18* (2), 1366-1372.
43. Lafeta, L.; Cadore, A. R.; Mendes-de-Sa, T. G.; Watanabe, K.; Taniguchi, T.; Campos, L. C.; Jorio, A.; Malard, L. M., Anomalous Nonlinear Optical Response of Graphene Near Phonon Resonances. *Nano letters* **2017,** *17* (6), 3447-3451.
44. Shutov, A. D.; Yi, Z.; Wang, J.; Sinyukov, A. M.; He, Z.; Tang, C.; Chen, J.; Ocola, E. J.; Laane, J.; Sokolov, A. V.; Voronine, D. V.; Scully, M. O., Giant Chemical Surface Enhancement of Coherent Raman Scattering on MoS2. *ACS Photonics* **2018,** *5* (12), 4960-4968.

TOC Graphics